

Paper

Int'l J. of Aeronautical & Space Sci. 16(3), 380–393 (2015)

DOI: <http://dx.doi.org/10.5139/IJASS.2015.16.3.380>

Performance evaluation method of homogeneous stereo camera system for full-field structural deformation estimation

Jong-Min Yun*, **Ho-Young Kim*** and **Jae-Hung Han****

Department of Aerospace Engineering, Korea Advanced Institute of Science and Technology (KAIST), 291 Daehak-ro, Yuseong-gu, Daejeon 34141, Korea

Hong-Il Kim*** and **Hyuk-Jun Kwon*****

Agency for Defense Development (ADD), 488 Bugyuseong-daero, Yuseong-gu, Daejeon 34188, Korea

Abstract

This study presents how we can evaluate stereo camera systems for the structural deformation monitoring. A stereo camera system, consisting of a set of stereo cameras and reflective markers attached on the structure, is introduced for the measurement and the stereo pattern recognition (SPR) method is utilized for the full-field structural deformation estimation. Performance of this measurement system depends on many parameters including types and specifications of the cameras, locations and orientations of them, and sizes and positions of markers; it is difficult to experimentally identify the effects of each parameter on the measurement performance. In this study, a simulation framework for evaluating performance of the stereo camera systems with various parameters has been developed. The maximum normalized root-mean-square (RMS) error is defined as a representative index of stereo camera system performance. A plate structure is chosen for an introductory example. Its several modal harmonic vibrations are generated and estimated in the simulation framework. Two cases of simulations are conducted to see the effects of camera locations and the resolutions of the cameras. An experimental validation is carried out for a few selected cases from the simulations. Using the simultaneous laser displacement sensor (LDS) measurements as the reference, the measurement errors are obtained and compared with the simulations.

Key words: stereo pattern recognition (SPR), stereo camera system, simulation framework, structural deformation estimation

1. Introduction

There has been a growing interest in the use of homogeneous stereo camera systems for the structural deformation measurement. Compared with other indirect shape estimation methods that utilize built-in strain sensors or accelerometers [1, 2], estimation with a homogeneous camera system is non-intrusive and robust since it's a non-contact type method. In addition, it is superior to other non-contact methods, such as those using laser displacement sensors (LDS), because it is capable of a full-field measurement with the use of only a single set of sensors. Owing to these advantages, its application ranges from the

deflection estimation of laboratory test structure model [3,4] to various maneuvering structures such as aircraft wings [5-7], rotor blades [8-10] and civil infrastructures [11-14].

Stereo Pattern Recognition (SPR) refers to a method using stereo camera and corresponding target object for deformation measurement. It uses objects such as reflective marker attached on the surface of the estimated structure to obtain deformation of the structure. The recovered spatial positions of objects on the target structure are chosen to represent the displacement of the target on marker location points [9]. Recently, even in-door navigation system based on SPR became available [15]. SPR method imposes less physical limitations than strain-gauge based or FBG based method while it guarantees enough data

This is an Open Access article distributed under the terms of the Creative Commons Attribution Non-Commercial License (<http://creativecommons.org/licenses/by-nc/3.0/>) which permits unrestricted non-commercial use, distribution, and reproduction in any medium, provided the original work is properly cited.

© * Ph. D Candidate
** Professor, Corresponding author: jaehunghan@kaist.ac.kr
*** Senior Researcher

quality compared with those methods [7].

On the other hand, in spite of the fact that the measurement performance of vision-based structure estimation system strongly depends on various parameters such as camera installation position, orientation, specifications and shape or dimension of the target object, studies which show quantitative relationship between these factors and the SPR system performance have rarely been reported. Several studies have performed regarding evaluation of spatial data quality of vision-based measurement system depending on marker shape. [16, 17] But those studies do not consider the performance dependency regarding camera parameters, and do not fully consider target structure properties for their simulation.

Varying one factor of SPR system while others keep fixed, it would be possible to experimentally investigate the effect of varying factors to the performance of the system. But it would be much better to have a simulation framework to evaluate the performance of SPR system since it is much more convenient compared with experiment and some factors such as sensor resolution or position are limited in the laboratory environment. In this study, to deal with these problems, a simulation framework using Matlab software is developed to predict the performance of SPR system depending on various related parameters. Some numerical examples are taken to show the effectiveness of the developed simulation framework. This study considers only homogeneous stereo camera set, which consists of two identical cameras, because homogeneous stereo camera set is the most widely used in SPR system application. The upcoming part of this paper organized as follows: In Section 2, theoretical fundamentals regarding reconstruction of object position using stereo camera are presented. In Section 3, the developed simulation framework for SPR system performance prediction is introduced; core parts of the framework and the overall procedure of the simulation using this framework are described. Section 4 presents some application examples of the framework using a thin plate target structure. Two different simulations are considered; one studies performance with varying camera position, and the other studies performance with varying camera resolution. Finally, parts of simulation cases are also experimentally studied and the result verifies the usefulness and validity of the developed framework.

2. Theoretical Background

2.1 Stereo Camera system concept

A camera is a device which projects object in 3-dimensional (3D) space to its 2-dimensional (2D) image plane, as shown

in Fig. 1. Since this projection makes all the objects on the same line toward the camera appear to be a single point, the depth information would be lost. That is why we cannot use a single camera to obtain 3D location of an object.

When an object image is taken by a stereo camera set (Fig. 2), two different projection points are obtained. Therefore, if the relationships between the object and each projection point, and the correspondence of projection points with each other are known, 3D position of the object is obtained with recovered depth value of it.

Projection point on camera image plane is related to 3D object by using camera projection matrix.

As it can be seen in Fig. 1, the object representation in camera center coordinate is given by equation (1).

$$\begin{Bmatrix} X^C \\ Y^C \\ Z^C \\ 1 \end{Bmatrix} = \begin{bmatrix} R_{3 \times 3}^T & 0 \\ 0 & 1 \end{bmatrix} \begin{bmatrix} I_{3 \times 3} & -T_{3 \times 1} \\ 0 & 1 \end{bmatrix} \begin{Bmatrix} X^O \\ Y^O \\ Z^O \\ 1 \end{Bmatrix} \quad (1)$$

where superscript O represents the object coordinate, C represents the camera coordinate, $R_{3 \times 3}$ is the rotation matrix and $T_{3 \times 1}$ is the translation vector as given in equation (2).

$$R_{3 \times 3} = R_z(\psi)R_y(\theta)R_x(\phi), \quad T_{3 \times 1} = \begin{Bmatrix} X_c^O \\ Y_c^O \\ Z_c^O \end{Bmatrix} \quad (2)$$

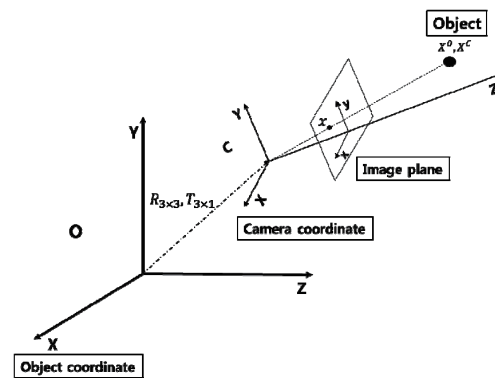


Fig. 1. Coordinate geometry of camera and object

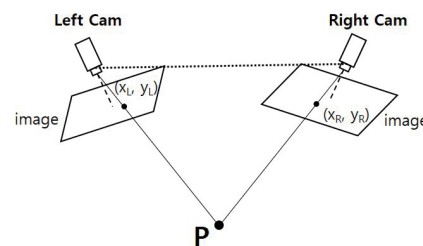


Fig. 2. Image taken by stereo camera set

Rotation matrix in each direction is given in equation (3).

$$R_x(\phi) = \begin{bmatrix} 1 & 0 & 0 \\ 0 & \cos \phi & -\sin \phi \\ 0 & \sin \phi & \cos \phi \end{bmatrix}, R_y(\theta) = \begin{bmatrix} \cos \theta & 0 & \sin \theta \\ 0 & 1 & 0 \\ -\sin \theta & 0 & \cos \theta \end{bmatrix}, \quad (3)$$

$$R_z(\psi) = \begin{bmatrix} \cos \psi & -\sin \psi & 0 \\ \sin \psi & \cos \psi & 0 \\ 0 & 0 & 1 \end{bmatrix}$$

The relationship between the projection point on the camera image plane and the camera coordinate is specified as follows:

$$\lambda \begin{bmatrix} x^{c,i} \\ y^{c,i} \\ 1 \end{bmatrix} = \begin{bmatrix} \gamma f & sf & x_0^{c,i} \\ 0 & f & y_0^{c,i} \\ 0 & 0 & 1 \end{bmatrix} \begin{bmatrix} 1 & 0 & 0 \\ 0 & 1 & 0 \\ 0 & 0 & 1 \end{bmatrix} \begin{bmatrix} X^c \\ Y^c \\ Z^c \\ 1 \end{bmatrix} = K \begin{bmatrix} X^c \\ Y^c \\ Z^c \\ 1 \end{bmatrix} \quad (4)$$

where γ is the CCD pixel aspect ratio, s is the CCD pixel skew, (x_0, y_0) is the CCD center point, K is the camera matrix, and superscript c, i refers to the camera image plane.

Substituting equation (1) to the right hand side of equation (4) gives the relationship between projection point and the object.

$$\lambda \begin{bmatrix} x^{c,i} \\ y^{c,i} \\ 1 \end{bmatrix} = KR_{3 \times 3}^T [I_{3 \times 3} | -T_{3 \times 3}] \begin{bmatrix} X^o \\ Y^o \\ Z^o \\ 1 \end{bmatrix} = P \begin{bmatrix} X^o \\ Y^o \\ Z^o \\ 1 \end{bmatrix} \quad (5)$$

where P is the camera projection matrix, which contains both intrinsic and extrinsic parameters of the camera. In CCD camera model, K -matrix is defined as

$$K_{cam} = \begin{bmatrix} -fm_x & 0 & x_0^{c,i} m_x \\ 0 & -fm_y & y_0^{c,i} m_y \\ 0 & 0 & 1 \end{bmatrix} \quad (6)$$

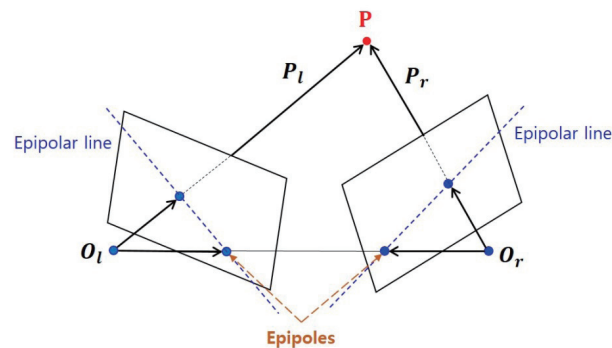


Fig. 3. Epipolar geometry for stereo matching

where m_x, m_y are pixel ratios in x and y direction, respectively.

Through equations (1) to (6), the relationship between the object and the projection point is established. In order to recover 3D position of the object, correspondence between two projection points should be verified; this is called stereo matching. To find the matching between two projection points, the concept of epipolar geometry is applied.

Restriction equation imposed by fundamental matrix between two cameras is used to check the correspondence of two projection points.

$$x_1^T F_{12} x_2 = 0 \quad (7)$$

where x_1 is the projection point on camera 1, x_2 is the projection point on camera 2, F_{12} is the fundamental matrix between camera 1 and 2.

2.2 Displacement calculation method

For two corresponding projection points of the object, 3D position of it is recovered using linear triangulation method [18].

By using P -matrix, relation between the object point X in 3D space and its projected point on camera image plane is given as

$$\lambda x_h = \lambda \begin{bmatrix} x \\ y \\ 1 \end{bmatrix} = PX = \begin{bmatrix} P_1^T \\ P_2^T \\ P_3^T \end{bmatrix} X \quad (8)$$

where P_i is i th column of the P matrix.

Assume n cameras are used to take an image of target object. Eliminating λ in the above equation and combine relationships from n camera gives systems of equation as

$$\begin{bmatrix} x_1 P_{31}^T - P_{11}^T \\ y_1 P_{21}^T - P_{11}^T \\ \vdots \\ x_n P_{3n}^T - P_{1n}^T \\ y_n P_{2n}^T - P_{1n}^T \end{bmatrix} X = 0 \quad (9)$$

Finally, 3D position of the target object is obtained by calculating the null space of it.

$$X_{est} = null \begin{bmatrix} x_1 P_{31}^T - P_{11}^T \\ y_1 P_{21}^T - P_{11}^T \\ \vdots \\ x_n P_{3n}^T - P_{1n}^T \\ y_n P_{2n}^T - P_{1n}^T \end{bmatrix} \quad (10)$$

3. Spr System Simulation Framework

The performance of the SPR system is dependent upon many parameters such as the positions, orientations, and the resolutions of cameras, as well as the geometry of the target structure and its vibration conditions. It would be very efficient if the measurement performance of the SPR system could be estimated in advance. We develop a simulation framework that enables us to see the effects of each parameter on the SPR performance. Fig. 4 summarizes the whole workflow of the framework.

Once the target structure is chosen, the first thing to be done in simulation procedure is the generation of its vibration data. The time histories of vibrating deflections at each nodal point are calculated by 'structure model part', using the modal data of the structure. Then marker locations as well as its specified shape and size need to be defined. Camera intrinsic parameters including the focal length, the resolution, the sampling frequency, and the charge-coupled device (CCD) sensor dimension are specified as well as the position and the orientation of cameras on 'camera model part'. Generated hypothetical stereo camera set measures the structural vibration during defined time span, using specific SPR algorithm in 'SPR algorithm model part'. Finally, the measurement error data is computed comparing the original structural vibration data and estimated vibration data by stereo camera set.

3.1 Generation of structure vibration data

In this framework, structure data based on the structure modal property is generated as follows:

As summarized in Fig. 5, after the mode shape data on each nodal point are obtained, a linear time invariant (LTI) simulation is performed based on the system of equations of

motion [19] with specified sampling frequency, during the specified time span. For the LTI simulation, acting point and equation of the force should be specified.

3.2 Realization of camera

To realize the process of camera to recognize the object and process the image of it, the object is realized by its dimension and specified number of boundary points. (Fig. 6) Using this boundary point realization, distortion and blurring of the object can be also realized.

Image capture by camera is realized via time synchronization of camera and structural data.

As shown in Fig. 7, structure image is taken during camera exposure time, on each camera sampling time. Then the obtained blurred image is processed to extract specific point.

Finally, to check whether the image is visible or not to camera, region of interest (ROI) has been checked as follows.

The equation (11) defines boundary of camera ROI.

$$Ax + By + C = 0 \tag{11}$$

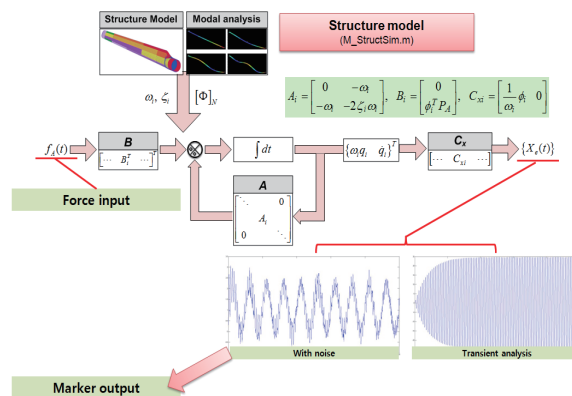


Fig. 5. Workflow of structure model part

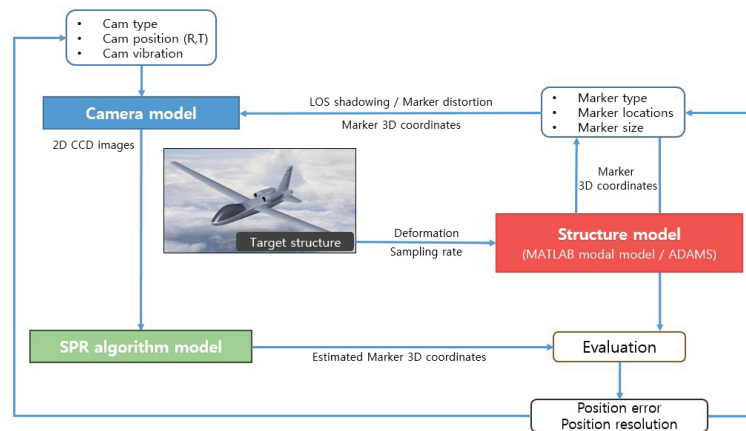


Fig. 4. Workflow of SPR system simulation framework

For the four boundary lines, constant of each line is specified by equation (12).

$$A_i = -(y_{i+1} - y_i), B_i = x_{i+1} - x_i, C_i = -(A_i x_i + B_i y_i) \quad (12)$$

Then, if the point x_p locates inside this ROI, it satisfies the equation (13).

$$D = A_i x_p + B_i y_p + C_i > 0 \quad (13)$$

For an object to be considered fully captured by the camera, all the boundary points of it should satisfy the equation (13).

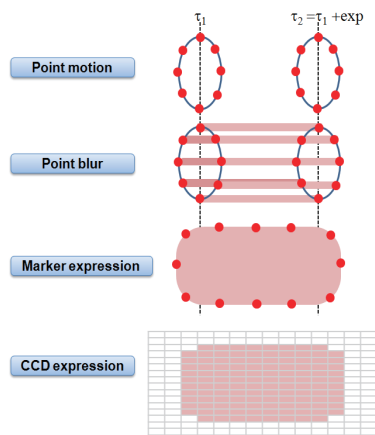


Fig. 6. Marker realization using boundary points

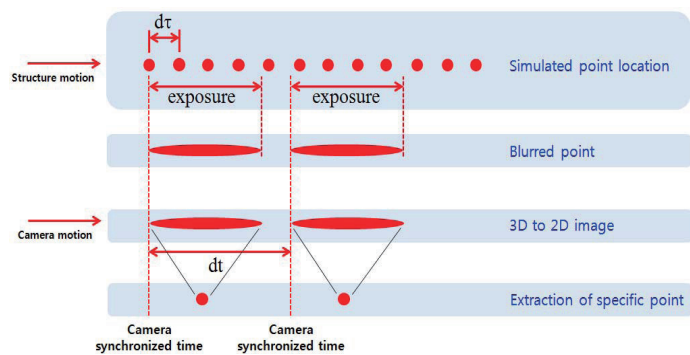


Fig. 7. Time synchronous of camera data and structure data

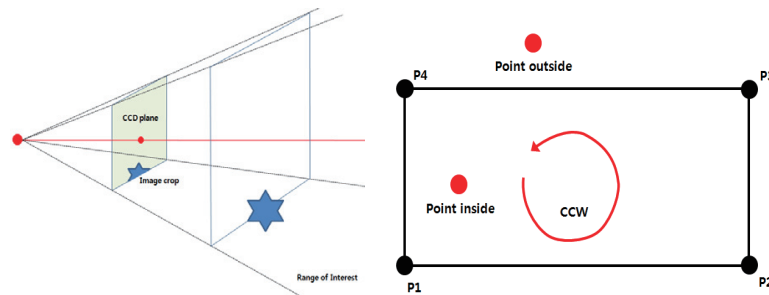


Fig. 8. ROI check of an object

3.3. Error definition for performance evaluation

In order to systematically evaluate the performance of SPR system, the definition of appropriate measurement error criteria is very important. The point-wise error in each direction, at nodal point k at time instance t is defined as equation (14).

$$er_\gamma(k, t) = \widehat{H}_\gamma(k, t) - H_\gamma(k, t) \quad (14)$$

where H_r is the reference structural shape, \widehat{H}_γ is the estimated structural shape.

But this point-wise error rarely tells anything regarding the overall performance of the SPR system. Therefore, the structural root-mean-square (RMS) errors for total direction and in single direction at time step t are respectively defined as

$$E_{RMS, total}(t) = \sqrt{\frac{\sum_{\gamma=1}^3 \{er_\gamma(t)\}^T \{er_\gamma(t)\}}{N}} \quad (15)$$

$$E_{RMS, \gamma}(t) = \sqrt{\frac{\{er_\gamma(t)\}^T \{er_\gamma(t)\}}{N}}$$

where N is the number of the used nodal points, and $\{er_\gamma(t)\} = \{er_\gamma(1, t), er_\gamma(2, t), \dots, er_\gamma(N, t)\}^T$ is an error vector in each direction.

This RMS error is normalized with respect to the maximum nodal deformation, for the whole time span.

$$E_{NRMS,total}(t) = \frac{E_{RMS,total}(t)}{\max_t \left(\sqrt{\sum_{\gamma=1}^3 \{D_{\gamma}(t)\}^T \{D_{\gamma}(t)\}} \right)}, \quad (16)$$

$$E_{NRMS,\gamma}(t) = \frac{E_{RMS,\gamma}(t)}{\max_t \left(\sqrt{\{D_{\gamma}(t)\}^T \{D_{\gamma}(t)\}} \right)}$$

where $\{D_{\gamma}(t)\}$ is structural deformation at time step t.

$E_{NRMS,total}(t)$ and $E_{NRMS,\gamma}(t)$ are respectively called total Normalized RMS Error (NRE), and directional NRE. In this paper, the worst values of $E_{NRMS,total}(t)$ or $E_{NRMS,\gamma}(t)$ are used to represent the eventual performance of each SPR system configuration.

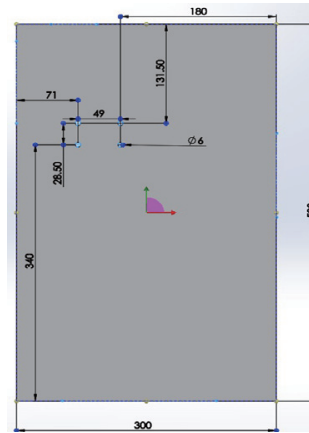


Fig. 9. Dimensions of the plate and the fixing points

4. APPLICATION EXAMPLE

4.1 Target structure

In order to facilitate the experimental study, a thin rectangular acrylic plate model is selected as target structure, in this study. The dimension and the material properties are given in Table 1, and Fig. 9 shows the fixing points of the plate.

An Impact test is performed to obtain modal frequencies of the plate. Using roving-sensor, fixing-excitation impact test method, impact test are performed on the seven

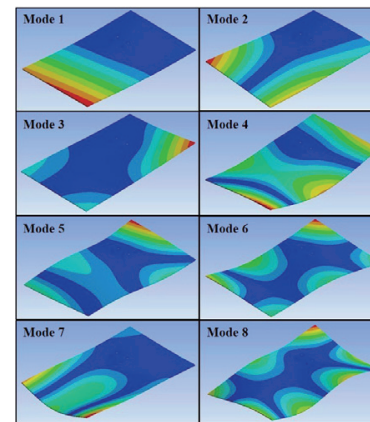


Fig. 10. Mode shapes up to 8th mode

Table 1. Determined plate geometry and material properties

Width (a) [mm]	Height (b) [mm]	Thickness (T) [mm]
300	500	3
Density [kg/m^3]	Young's Modulus [GPa]	Poisson ratio
1130.00	3.12	0.37

Table 2. Natural frequency from analysis and experiment

Mode number	Natural Frequency (Hz)		
	Analysis	Experiment	Error (%)
1	6.37	6.36	0.16
2	14.340	15.38	6.76
3	24.58	24.38	0.82
4	33.77	31.19	8.27
5	48.08	38.56	24.69
6	55.51	54.44	1.97
7	68.28	63.75	7.11
8	75.91	82.19	7.64

different sensor and excitation location sets, not to miss any vibrational modes. The modal frequency data are compared to the modal frequency result obtained from the ANSYS analysis in Table 2, showing the good agreements except the 5th mode. Fig. 10 shows the mode shapes obtained from ANSYS analysis.

Modal data up to 6th mode has used for structural data generation. Equally distributed 58 points on the surface are selected for the marker points as shown in Fig. 11. Three directional mode shape data for these points from the modal analysis by ANSYS 15.0 are extracted for the structural data generation.

4.2 SPR system performance evaluation

Among various parameters of SPR camera system, the effects of position and the resolution of stereo cameras are focused in this paper. Only the homogeneous stereo camera system, which consists of two identical cameras, is considered. As described earlier, equally distributed 58 markers are used; the number of the markers is enough to recover the deformation field of the whole structure.

Two kinds of examples are presented. First example studies the effects of camera positions; for a set of homogeneous stereo camera set, the performance evaluation is conducted according to varying camera position while fixing the distance from the plate center point.

This would help to grasp the general idea of suitable relative location of the stereo camera set. Second example deals with the performance evaluation of homogeneous stereo camera set with fixed position and orientation according to varying camera resolution. For both cases, performance is evaluated for three structural vibrations, which are 1st, 2nd and 6th mode harmonic vibrations with constant maximum amplitude (Table 3), for 1 second.

4.2.1 First simulation case

In first case, camera position is varying on the surface of 2.5b radius hemisphere, with the condition that two cameras

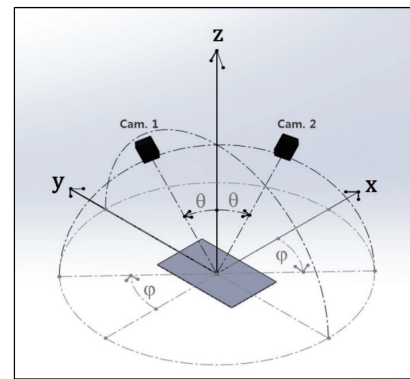


Fig. 12. Simulation case 1 : Camera moving on the sphere with radius 2.5b

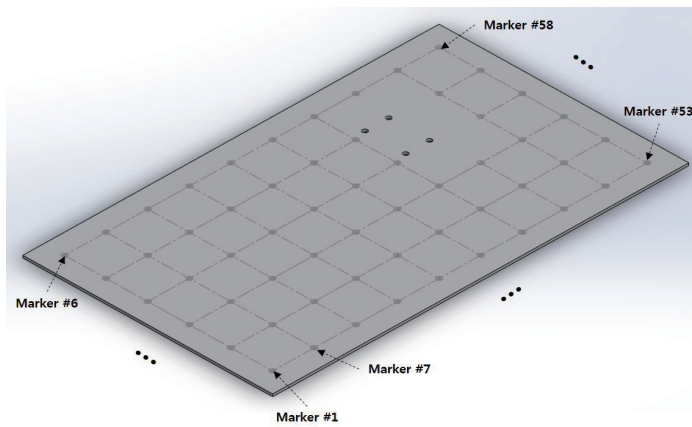


Fig. 11. Marker points of the plate

Table 3. Structure vibration cases

Case number	Structure vibration cases	Equation
1	Mode 1	$10T \times \sin(2\pi f_1 t) \times \{ \psi_1(k) \}$
2	Mode 2	$10T \times \sin(2\pi f_2 t) \times \{ \psi_2(k) \}$
3	Mode 6	$10T \times \sin(2\pi f_6 t) \times \{ \psi_6(k) \}$

should be in symmetry with respect to Z axis.

There should be an upper bound on elevation angle θ because adjacent markers start to overlap as elevation angles become large. Considering the marker image projected to both camera image plane at elevation angle of 80° as shown in Fig. 13, elevation angle is restricted be less than 80 degree.

The position of each camera is specified in spherical coordinates, $(r, \theta, \varphi) = (2.5b, \theta, \varphi)$, where the elevation and azimuth angle ranges are $5^\circ \leq \theta < 80^\circ$, $0^\circ \leq \varphi \leq 90^\circ$, respectively. The simulation is performed for every 5° interval of both elevation and azimuth angles.

The intrinsic parameters are kept same for the all cases, and those are summarized in Table 4.

Figures 14 - 16 show the maximum total NRE for varying elevation angles at the azimuth angle of 45° , for three vibration cases.

The result shows that the maximum total NRE minimizes when the cameras are located at mid-altitude. This result can be considered as reasonable, because z directional measurement accuracy increases as cameras location lowered (high elevation angle), x or y directional measurement accuracy increases as cameras locations are getting higher (low elevation angle). This expectation is



Fig. 13. Markers projected on both camera image plane, at $\theta=80^\circ$

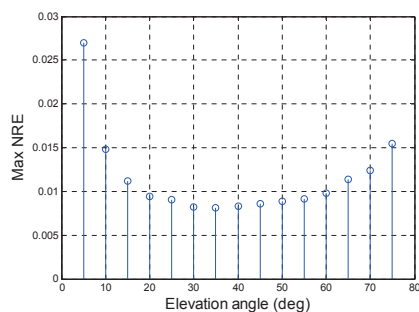


Fig. 14. Maximum total NRE at $\varphi=45^\circ$, for vibration mode 1

Table 4. Camera intrinsic parameters for simulation case 1

Sensor type	Focal length (mm)	Resolution (pixels)
CCD	6	1280×1024
Pixel size (μm)	Frame rate (Hz)	Exposure time (ms)
4.8	240	1.0

clarified in Fig. 17. The RMS error without normalization is shown because maximum deformation in x and y direction is too small compared to the maximum deformation in z direction (about 100 times smaller), normalized error does not give meaningful result.

Therefore in total, when the all three directions are considered, the measurement accuracy is maximized when the cameras are located at middle altitude (middle elevation

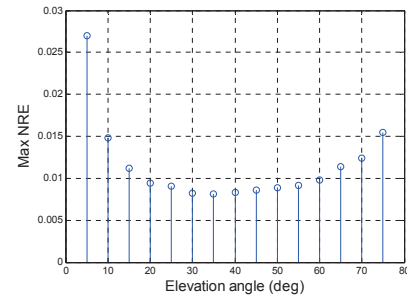


Fig. 15. Maximum total NRE at $\varphi=45^\circ$, for vibration mode 2

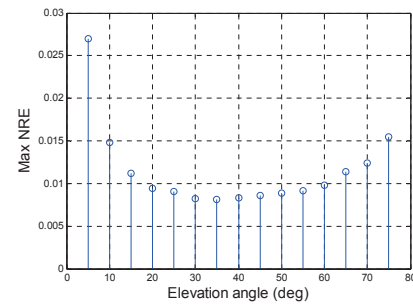


Fig. 16. Maximum total NRE at $\varphi=45^\circ$, for vibration mode 6

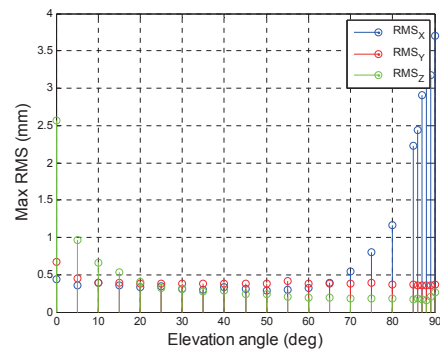


Fig. 17. Maximum directional RMS error at $\varphi=45^\circ$, for vibration mode 1

angle).

To find the best position of camera for each vibration case, elevation angles that minimize the maximum total NRE value are found for every azimuth angle. The result is as shown in Fig. 18.

In all azimuth angle cases, the best camera position lies in the range of 30° to 50° of elevation angle. For each vibration case, the best positions of stereo camera set, when the distance from the plate center is fixed to 2.5b, are summarized in Table 5.

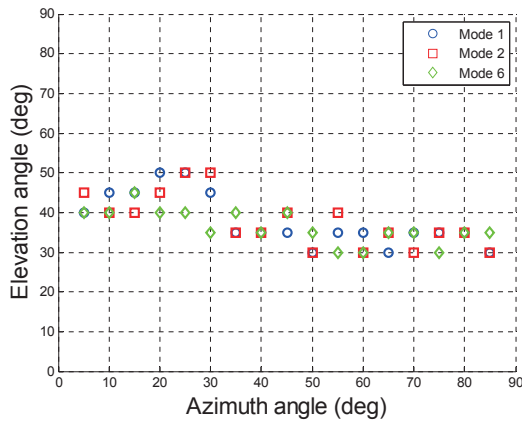


Fig. 18. Best elevation angles with respect to azimuth angle

Table 5. Best camera position for each vibration case

Structure vibration case	Best position (φ, θ)
Mode #1	(35°, ±40°)
Mode #2	(40°, ±55°)
Mode #6	(40°, ±45°)

4.2.2 Second simulation case

In second case, positions of both camera are set to $(x, y, z) = (\pm 2a, -4b, 2b)$, as shown in Fig. 19. Note that, in many practical measurement cases, the available camera installation positions are limited. This example studies the effects of varying resolution of the cameras on the SPR measurement performance.

Camera intrinsic parameters except the resolution are kept the same as in simulation 1. The positions and orientations of both cameras are set to be the values listed in Table 6.

The resolutions of both cameras are changed while keeping pixel sizes are the same in both directions. Fig. 20 shows how the obtained 2D images can be affected by the camera resolution, and we can easily expect the measurement accuracy drops as the resolution decreases.

Table 7 provides quantitative measures for the effects of the camera resolutions. It is found that the maximum total NRE value increases linearly with increasing pixel size. This trend is clearly shown in Fig. 21. The maximum total NRE is also dependent on vibration types. In all seven resolution

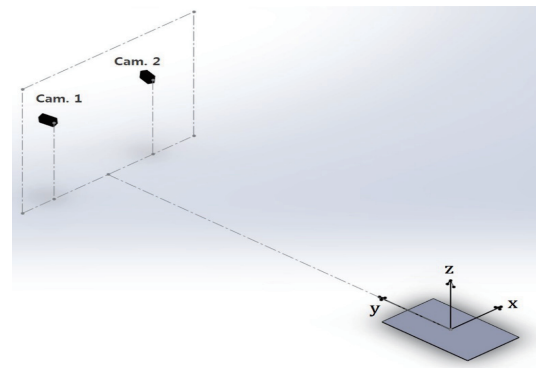


Fig. 19. Simulation case 2 : Camera position fixed

Table 6. Position and orientation of both cameras

	Position (mm)			Orientation (deg)		
	X	Y	Z	R_x	R_y	R_z
Camera 1	-600	-2000	1000	-110	12.5	0
Camera 2	600	-2000	1000	-110	-12.5	0

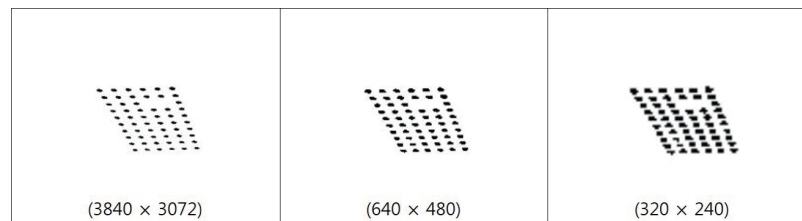


Fig. 20. Projection image with varying resolution

cases, maximum total NRE increases slightly for higher modes. From this kind of analysis, one can wisely choose the necessary cameras once the required measurement performance level is decided. Compromise between measurement performance and the camera resolution could

be made because the camera resolution is directly related to camera cost.

4.3 Experimental works

Experimental works are conducted for some of the first simulation cases. Two identical cameras (Model no. : Prime 13W, *OptiTrack*) are used to configure stereo camera set. Each camera is equipped with IR band-pass filter with wavelength of $[850\pm 10]nm$. The detailed camera specification is given in Table 8.

(1) Effect of camera position

The position of two selected markers are measured simultaneously using two identical laser displacement sensor (LDS) s (Model no. : LK-G400, *Keyence*). This data is used as a reference shape estimation data.

Experiments are conducted for eight position cases, as specified in Table 9.

Using function generator, the plate is vibrated with the

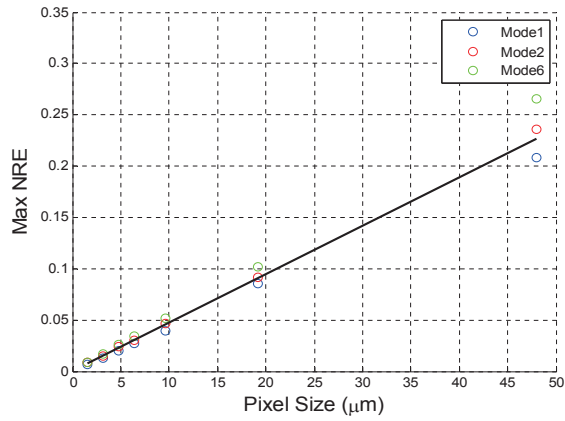


Fig. 21. Maximum total NRE with respect to pixel size

Table 7. Simulation 2 result

Resolution (pixel × pixel)	Pixel size (μm)	Maximum total NRE (%)		
		Mode 1	Mode 2	Mode 6
3840 × 3072	1.6	0.70	0.82	0.90
1920 × 1440	3.2	1.33	1.52	1.72
1280 × 1024	4.8	1.99	2.42	2.58
960 × 720	6.4	2.67	3.05	3.40
640 × 480	9.6	3.97	4.70	5.14
320 × 240	19.2	8.49	9.18	10.21
128 × 108	48.0	20.78	23.61	26.56

Table 8. Camera specifications, *OptiTrack* Prime 13W

Sensor type	Focal length (mm)	Resolution (pixel)	Pixel size (μ m)
CCD	3.5	1280 × 1024	4.8
Frame rate (Hz)	Field of view	Exposure time (ms)	Interface
240	82°X70°	1.0	GigE/PoE (Data) Ethernet (Camera Sync)

Table 9. Camera Position & orientation for experiment

	Position			Orientation (deg)		
	R (mm)	θ (°)	φ (°)	R_x (°)	R_y (°)	R_z (°)
Camera 1	750	[-20, 30, 40, 45, 50, 60, 70]	0	180	$-\theta$	0
Camera 2	750	[20, 30, 40, 45, 50, 60, 70]	0	180	θ	0

1st natural frequency, which is 6.37Hz. Like the simulation, the plate in steady-state vibration is monitored for 1 second. From the simulation it is known that the overall performance trend is similar independent of vibration modes. Thus, only the validation experiment was performed for only the 1st mode vibration case. Furthermore, we only compare the direction NRE because it is very difficult to measure in-plane deformation (i.e. X and Y directions) with LDS. For each camera position, the same measurements (both LDS and SPR) are repeated for ten times to obtain ensemble averages of the measurements. Then the error is calculated by comparing these two data. An example of comparison of the measurement results is shown in Fig. 23, for $\theta=60^\circ$ case, for the marker #1 and #6.

In Fig. 24, the calculation of maximum NRE in z-direction for the eight elevation angle cases is shown, and compared to the result from the simulation.

The z-directional NREs from the experiment are in the range of 1.5% to 4%, and the elevation angle range of $45^\circ \sim 60^\circ$ are found to be good to have low maximum z-directional NRE. While the tendency of varying NREs according to the elevation angle change looks similar, the NREs from experiments are generally higher than the simulation cases; the main reason is the reference structural shape in the experiment is obtained from other sensors that also contain

certain level of measurement errors.

(2) Full-field shape estimation

To see the full-field shape estimation capability, the plate under sine sweep vibratory excitation force is monitored. Using the shaker shown in Fig. 22, sine sweep function with varying frequency from 0 to 55Hz in 10 seconds is used to vibrate the plate. The vibration shape of the plate is reconstructed using the same stereo camera set (Table 8); the positions of both cameras are set to $(1.5b, \pm 20^\circ, 0^\circ)$ in spherical coordinates. With the marker configuration given

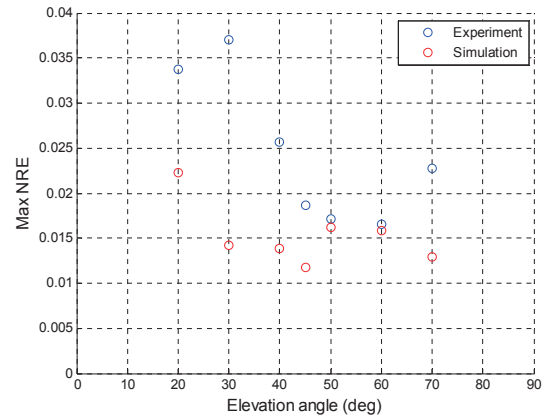


Fig. 24. Z-directional NRE comparison from experiment and simulation

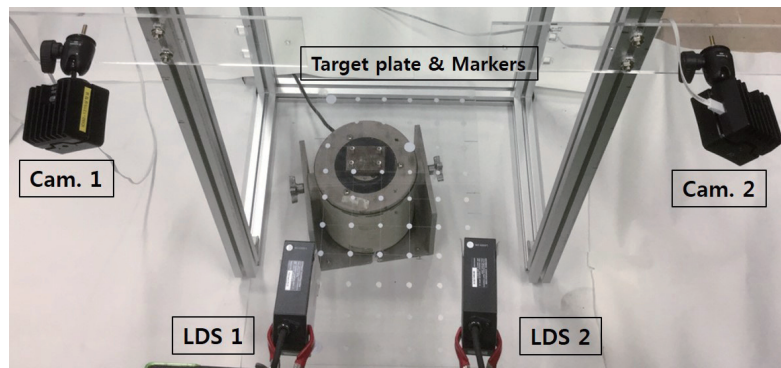


Fig. 22. Experiment configuration

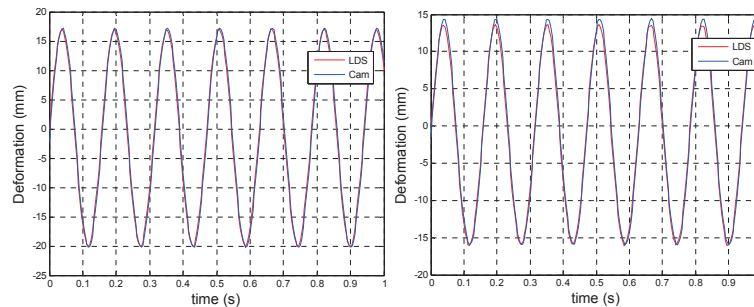


Fig. 23. Comparison of measurement results, at marker #1 (left), marker #6 (right)

in Fig. 11, time-history of the deformation measurement result in z-direction on two representative marker points, the one with the largest deformation and the other with the smallest deformation, are given in Fig. 25.

The full-field measurement result at two time steps as shown in Fig. 25, is presented in Figs. 26 and 27. Full-field deformation images of the target plate are recovered by interpolating the position values obtained at 58 marker

points. Note that the scale of magnitude color bar is different in Figs. 26 and 27; it is adjusted for more clear contrast. At the first time step selected, t_1 , the deformation has its maximum value; the plate vibrates with its first mode. As expected, the deformation image in Fig. 26 is very close to the 1st mode shape shown in Fig. 10. Fig. 27 shows the snap shot of the deformation of the plate at the time step t_2 .

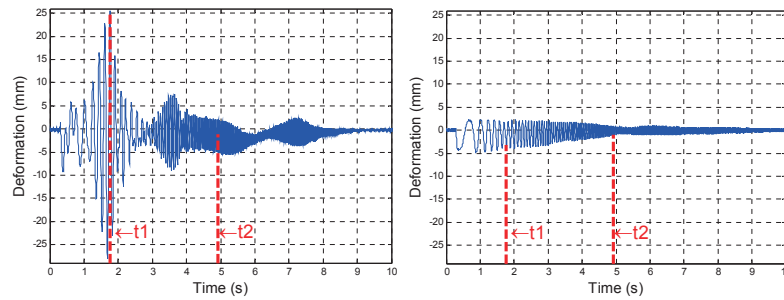


Fig. 25. Deformation measurement result at marker #1 (left), marker #41 (right)

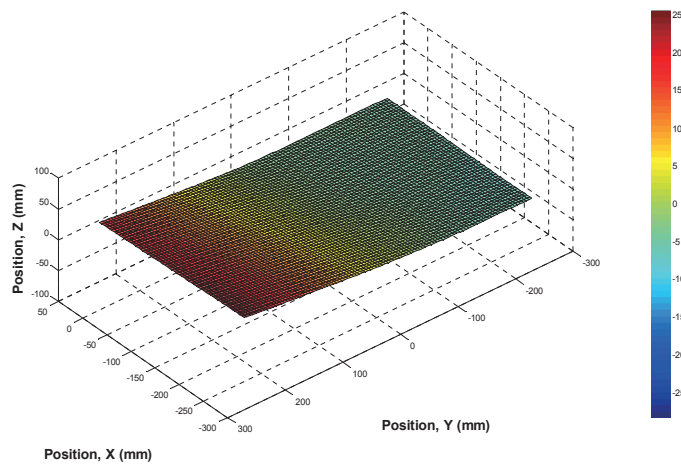


Fig. 26. Full-field deformation measurement result at time step t_1

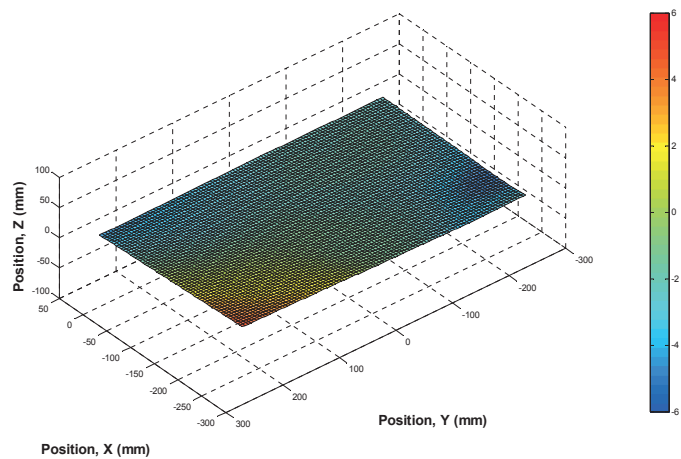


Fig. 27. Full-field deformation measurement result at time step t_2

5. Conclusion

In this paper, a simulation framework for the performance evaluation of a stereo camera system has been developed. Using the developed simulation framework, we analyzed the performances of SPR system for two cases with a rectangular plate structure as the target structure. The first one deals with varying camera position with camera-to-plate-center distance held constant, the other studies the effects of varying camera resolution with fixed position and orientation of cameras. For both simulation cases, three vibration cases of the plate are monitored. From the result of the first study, the performance of the shape reconstruction, which is measured by maximum total NRE, is found to be better when the stereo camera set is positioned at the medium altitude. The position is expressed using spherical coordinates for convenience, and the best positions are found to be in around 35°~ 40° in elevation angle which implies medium altitude. From the second simulation, the performance of the stereo camera set decreases linearly as its resolution decreases when all the other parameters are kept constant. SPR system is constructed and two cases of experiments are conducted. The first experiment is to verify the best camera positions found from the first simulation. Similar to the simulation results, the mid altitude camera positions, which is 45° of elevation angle, gives the best performance; however, the overall error levels are larger than those of the simulation because of uncertainties in experiment such as the measurement errors of the reference signals and camera calibration errors. The second experiment aims to show the applicability of the stereo camera system to full-field deformation measurement. With cameras set on the proper position in the performance sense, full-field measurability of stereo camera system is tested on the structure under sine sweep vibratory force. This, together with the first experiment result, validates the usefulness and effectiveness of the developed framework.

Acknowledgment

This study is supported by a research program of Agency for Defense Development (ADD) under the contract UD130027JD.

References

[1] Kim, H.-I., Kang, L.-H. and Han, J.-H., "Shape estimation with distributed fiber Bragg grating sensors for

rotating structures", *Smart Materials and Structures*, Vol. 20, No. 3, 2011, 035011.

[2] Djurić-Jovičić, M. D., Jovičić, N., and Popović, D. B., "Kinematics of Gait: New Method for Angle Estimation Based on Accelerometers", *Sensors*, Vol. 11, No. 11, 2011, pp. 10571-10585.

[3] Kim, H.-I., Kim, H.-Y., Park, H.-J. and Han, J.-H., "Development of a Point Tracking System for Measuring Structural Deformations Using Commercial Video Cameras", *International Journal of Aeronautical and Space Sciences*, Vol. 10, No. 2, 2009, pp.86-94.

[4] Wu, L.-J., Casciati, F. and Casciati, S., "Dynamic testing of a laboratory model via vision-based sensing", *Engineering structures*, Vol. 60, 2014, pp. 113-125.

[5] Kurita, M., Koike, S., Nakakita, K. and Masui, K., "In-Flight Wing Deformation Measurement", *51st AIAA Aerospace Sciences Meeting including the New Horizons Forum and Aerospace Exposition*, 07-10 January 2013, Grapevine (Dallas/Ft. Worth Region), TX, AIAA 2013-0967

[6] Yu, Y., Yang, Q. and Wang, X., "3D imaging application in the studies of micro air vehicles", *Computers in industry*, Vol. 64, No. 9, 2013, pp. 1178-1185.

[7] Pang, Z. Y., Cesnik, C. E. and Atkis, E. M., "In-Flight Wing Deformation Measurement System for Small Unmanned Aerial Vehicles", *55th AIAA/ASME/ASCE/AHS/SC Structures, Structural Dynamics, and Materials Conference*, 13-17 January 2014, National Harbor, MD, AIAA 2014-0330.

[8] van der Wall, B. G., Burley, C. L., Yu, Y. H., Richard, Y. H., Richard, H., Pengel, K. and Beaumier, P., "The HART II test - measurement of helicopter rotor wakes", *Aerospace Science and Technology*, Vol. 8, No. 4, 2004, pp. 273-284.

[9] Schneider, O., "Analysis of SPR measurements from HART II", *Aerospace Science and Technology*, Vol. 9, No. 5, 2005, pp. 409-420.

[10] Kim, D.-H., Kim, S.-H., Park, J.-W., and Han, J.-H., "Blade Deformation Measurement of a Model-Scale Rotor System Using a SPR system with IR cameras", *39th European Rotorcraft Forum*, 3-6 September 2013, Moscow.

[11] Kim, S.-W. and Kim, N.-S., "Multi-point Displacement response measurement of civil infrastructures using digital image Processing", *The Proceedings of the Twelfth East Asia-Pacific Conference on Structural Engineering and Construction*, Vol., 14, 2011, pp. 195-203.

[12] Lee, J. J. and Shinozuka, M., "A vision-based system for remote sensing of bridge displacement", *NDT & E International*, Vol. 39, No. 5, 2006, pp. 425-431.

[13] Ni, Y. Q., Wong, K. Y. and Xia, Y., "Health Checks through Landmark Bridges to Sky-high Structures", *Advances in Structural Engineering*, Vol. 14, No. 1, 2011, pp. 103-119.

[14] Lee, J.-H., Ho, H.-N., Shinozuka, M. and Lee, J.-J., "An

advanced vision-based system for real-time displacement measurement of high-rise buildings”, *Smart Materials and Structures*, Vol. 21, No. 12, 2012, 125019

[15] Kim, H.-Y., Lee, J.-S. and Han, J.-H., “Autonomous formation flight of multiple flapping-wing flying vehicles using motion capture system”, *Aerospace Science and Technology*, Vol. 39, No. 1, 2014, pp. 596-604.

[16] Lee, D., Jeon, H. and Myung, H., “Vision-based 6-DOF displacement measurement of structures with a planar marker”, *Smart Structures and Materials+ Nondestructive Evaluation and Health Monitoring, International Society*

for Optics and Photonics, 11-16 March 2012, San Diego, Proceedings of the SPIE Paper No. 834528.

[17] Jeon, H., Kim, Y., Lee, D. and Myung, H., “Vision-based remote 6-DOF structural displacement monitoring system using a unique marker”, *Smart Structures and Systems*, Vol. 13, No. 6, 2014, pp. 927-942.

[18] Hartley, R. I. and Strum, P., “Triangulation”, *Computer Vision and Image Understanding*, Vol. 68, No. 2, 1997, pp.146-157.

[19] Michael, R. H., *Vibration simulation using MATLAB and ANSYS*, Chapman & Hall, New York, 2001.